RSC Advances

PAPER

View Article Online
View Journal | View Issue

Open Access Article. Published on 02 January 2026. Downloaded on 1/21/2026 12:58:23 AM.
This article is licensed under a Creative Commons Attribution-NonCommercial 3.0 Unported Licence.

Check for updates

Cite this: *RSC Adv.*, 2026, **16**, 425

Ultrafast carrier dynamics and electronic properties of $PtSe_2/MoSe_2$ and WSe_2 2D TMDC layered structures on mica: combined THz spectroscopy and DFT study

Y. Samet Aytekin,[a] Céline Vergnaud,[c] Rahul Sharma,[c] Alain Marty,[c] Eleonora Pavoni,[d] Elaheh Mohebbi,[d] Emiliano Laudadio,[d] Matthieu Jamet,*[c] Davide Mencarelli,*[d] Hakan Altan*[b] and Okan Esenturk*[a]

A detailed investigation of structure, electronic and optical properties of two transition metal dichalcogenide (TMDC) structures is presented in this study. Sample 1 consists of epitaxially grown bilayer of $PtSe_2$ (2 monolayers) on $MoSe_2$ (1 monolayer) deposited on mica substrate – reported here for the first time. Sample 2 comprises a trilayer of WSe_2 grown on mica. The photoconductivities of both samples were characterized using optical pump-terahertz probe spectroscopy under above- and near-bandgap excitations at 400 nm and 800 nm. Both structures exhibit rapid carrier generation and relaxation dynamics, with notable variations depending on excitation wavelength and structures. Complementary density functional theory (DFT) calculations are performed to evaluate the electronic and optical properties of free-standing single layers of $MoSe_2$, $PtSe_2$ and WSe_2 and their combined structures corresponding to Sample 1 and Sample 2. The experimental results show strong agreement with calculated band structures. This consistency between experiment and theory underscores the potential of these TMDC structures for future applications in terahertz and high-frequency electronic devices.

Received 18th September 2025
Accepted 5th December 2025

DOI: 10.1039/d5ra07084h

rsc.li/rsc-advances

Introduction

The terahertz (0.1–10 THz) band offers increasing potential for applications, particularly in communications, where semiconductor-based sources face a fundamental trade-off between output power and bandwidth.[1] Therefore, broadband, high-power THz sources are essential for ultra-high data transfer rates. Beyond communications, they are also critical for industrial applications including ultrafast processing, high-resolution imaging, and biomedical and chemical sensing.[2,3] To advance in these areas, the new materials with suitable conduction properties to bridge the electronic gap to the terahertz frequency range are needed.

The exceptional optical and electrical properties of 2D materials are promising candidates as novel single-layer and van der Waals multilayer thin films. Notably, graphene shows strong potential due to its tunable properties.[4–7] The substrates, surface modifications, and metal contacts used with graphene can significantly alter its properties, posing challenges for its integration into large-scale optical devices.[8] Furthermore, no bandgap property limits its application in digital large-scale integrated circuits (ICs).[9] Attempts of generating a bandgap on graphene[10–12] have been rather indecisive due to the complex nature of the processes resulting in rather smaller bandgap and diminished mobility.[13,14]

Transition metal dichalcogenides (TMDCs) and monochalcogenides (TMMCs), on the other hand, possess unique properties in their 2D form. Even though they have indirect bandgap in their bulk form, the energy band structure changes to direct band gap as the layer number is decreased to one.[15–19] With their atomic thickness and absence of surface dangling bonds, these materials provide a new approach for building van der Waals (vdW) heterostructures.[20,21] Studies have shown that the electrical and chemical properties of these films can be significantly enhanced by doping and/or when grown in multilayer heterostructures. Various 2D single or multi-layered TMDCs have been studied for their distinct electrical and optical properties. In a study by Zhao *et al.* few layers of platinum diselenide ($PtSe_2$) showed semiconducting behavior with

[a]*Department of Chemistry, Middle East Technical University, Ankara, Turkey. E-mail: eokan@metu.edu.tr*

[b]*Department of Physics, Middle East Technical University, Ankara, Turkey. E-mail: haltan@metu.edu.tr*

[c]*Université Grenoble Alpes, CEA, CNRS, IRIG-Spintec, 38000 Grenoble, France. E-mail: matthieu.jamet@cea.fr*

[d]*Department of Sciences and Engineering of Matter, Environment and Urban Planning, Università Politecnica delle Marche, Ancona 60131, Italy. E-mail: d.mencarelli@staff.univpm.it*

© 2026 The Author(s). Published by the Royal Society of Chemistry

Open Access Article. Published on 02 January 2026. Downloaded on 1/21/2026 12:58:23 AM. This article is licensed under a Creative Commons Attribution-NonCommercial 3.0 Unported Licence.

a relatively high electron mobility of 210 $cm^2 V^{-1} s^{-1}$,[22] while the bulk form exhibited a metallic-like behavior with a conductivity of 6.20×10^5 S m^{-1}.[23] Iqbal *et al.* presented mobility and electrical characteristics of monolayer tungsten disulfide (WS_2) in a field effect transistor (FET) structure. The sandwiched WS_2 between hexagonal boron nitride (BN) films posed an advantage for fabricating stable WS_2 devices and also improved its mobility up to 214 $cm^2 V^{-1} s^{-1}$ at room temperature, and even as high as 486 $cm^2 V^{-1} s^{-1}$ at 5 K.[24] Fang *et al.* demonstrated high-performance p-type FET based on single-layer (0.7 nm thick) tungsten diselenide (WSe_2) with chemically doped source/drain contacts and high-κ gate dielectrics.[25] The top-gated monolayer WSe_2 transistors exhibit a high effective hole mobility of *ca.* 250 $cm^2 V^{-1} s^{-1}$, a perfect subthreshold swing of ~60 mV dec^{-1}, and an I_{ON}/I_{OFF} ratio of >10^6 at room temperature. Li *et al.* demonstrated that tuning the bandgap of TMDCs could be an approach for developing tunable nanoscale photoelectric devices operating at the near-infrared range. For that purpose, atomically thin, two-dimensional alloy MoS_{2x}-$Se_{2(1-x)}$ nanosheets with fully tunable chemical compositions and optical properties were synthesized using a simple one-step chemical vapor deposition approach.[26] In another study, Cheng *et al.* fabricated and characterized an atomically thin p–n diode based on a vertical heterojunction between p-type monolayer WSe_2 and n-type few-layer MoS_2.[27] The p–n junction was formed across the entire overlapping region of the WSe_2 and MoS_2 layers, achieving a high external quantum efficiency of up to 12%. The electroluminescence studies also showed prominent excitonic emission and enhanced hot-electron luminescence, providing insights into the electron–orbital interactions in these TMDC materials. These and other studies have laid the foundation for TMDCs to be considered as candidates for THz device architectures. Thus, characterization of their material parameters in the THz frequency range is a crucial step towards this goal.

Terahertz phase sensitive measurement capabilities offer a non-contact method of characterizing the electrical properties of such thin film structures. The technique has already been applied in numerous areas like biological systems,[28] semiconductors,[29] polymers,[30] active pharmaceutical ingredients,[31] for qualitative and quantitative analysis of the spintronic materials.[32] Time-resolved terahertz spectroscopy-TRTS, known as optical pump terahertz probe spectroscopy, on the other hand, is an advanced version that generates photoexcited quasiparticles and probes those particles with picosecond (ps) time resolution to asses dynamical behaviors.[33–35] In probing semiconducting thin films such as TMDCs and TMMCs, TRTS can directly measure intrinsic photoconductivity, track charge carrier behaviors along with phonon responses and intra-band transitions. Owing to its noncontact nature, THz-TDS allows to extract dielectric responses and frequency-dependent complex conductivity of 2D structures. The obtained THz response is analyzed in both time and frequency domains in order to conceive the fundamental physics of the ultrafast phenomena in these materials.[36] The initial rise and decay dynamics of the optically generated charge carriers enables to determine the carrier dynamics characteristics.[36] Docherty *et al.* studied the THz conductivity of CVD grown monolayer MoS_2 and WSe_2 on sapphire substrates with TRTS technique.[37] By optical pumping at resonance or with a photon energy above the bandgap, the monolayer semiconductor samples responded very rapidly demonstrating their potential to be used for the next generation high frequency optoelectronic devices, photoreceivers, emitters, and diodes.

In this study we present the structural and dynamical properties of two TMDC heterostructures: 1L $MoSe_2$ + 2L $PtSe_2$ on mica (Sample 1)-to our knowledge reported here for the first time- and 3L WSe_2 on mica (Sample 2). The films are grown on a large area (15 × 15 mm) by molecular beam epitaxy (MBE) in the vdW, regime.[38–40] The quality of the films are characterized by XRD, RHEED, AFM, and Raman, and their band structures were calculated and compared with THz measurements. Time-resolved charge carrier dynamics of the TMDC heterostructures are obtained by optical excitation at 400 nm or 800 nm with varying fluences and pump wavelength and fluence dependent fast relaxation dynamics are observed. The TMDC 2D films with such fast relaxations are good candidates for THz device applications and in high frequency optoelectronic devices. In addition, optical and electronic properties of 1L $MoSe_2$ and 1L $PtSe_2$, have been investigated by DFT. The same first principle analysis has also been used to evaluate the properties of 3L WSe_2 since the peculiarities of 1L WSe_2 were already studied.[41]

Experiments and methods

2L $PtSe_2$/1L $MoSe_2$ (Sample 1) and 3L of WSe_2 (Sample 2) are epitaxially grown on single crystalline 15 × 15 mm muscovite mica substrate (Ted Pella, Inc.). Mica is first exfoliated mechanically using Scotch tape to obtain a clean surface. Before its introduction into the ultrahigh vacuum (UHV) growth chamber, the substrate is exposed to a soft oxygen plasma to passivate its surface.[40] The base pressure in the MBE chamber remains in the low 10^{-10} mbar range. The mica substrate is first outgassed in the MBE chamber at 700 °C for 30 min to remove all the contaminants. $MoSe_2$, $PtSe_2$ and WSe_2 are grown by co-evaporating Mo, Pt and W respectively from an e-gun evaporator at a rate of 0.15 Å min^{-1} and Se from an effusion cell. The Se partial pressure measured at the sample position is fixed at 10^{-6} mbar. The growth temperature as given by a thermocouple in contact with the sample holder is 920 °C for $MoSe_2$ and WSe_2 while $PtSe_2$ is grown on $MoSe_2$ at a substrate temperature of 430 °C and then annealed at 725 °C during 6 minutes. *In situ* reflection high energy electron diffraction (RHEED) is used to monitor the crystal structure during the growth.

The absorption spectra of the samples were obtained by a Shimadzu 3600 plus UV-Vis-NIR spectrometer. Raman spectra were obtained by a homemade Raman system. The experimental THz-TDS and TRTS systems setup is presented in Fig. 1. The laser source was a Ti : Sapphire regenerative amplifier (Spitfire ACE, Spectra-Physics/Newport) with 5 mJ pulse energy, 1 kHz repetition rate, 60 fs pulse length, and a central wavelength of 800 nm. The beam is split into three; two of the beams (0.6 mJ) are used for THz generation and detection, whilst the

 © 2026 The Author(s). Published by the Royal Society of Chemistry

Open Access Article. Published on 02 January 2026. Downloaded on 1/21/2026 12:58:23 AM.
This article is licensed under a Creative Commons Attribution-NonCommercial 3.0 Unported Licence.

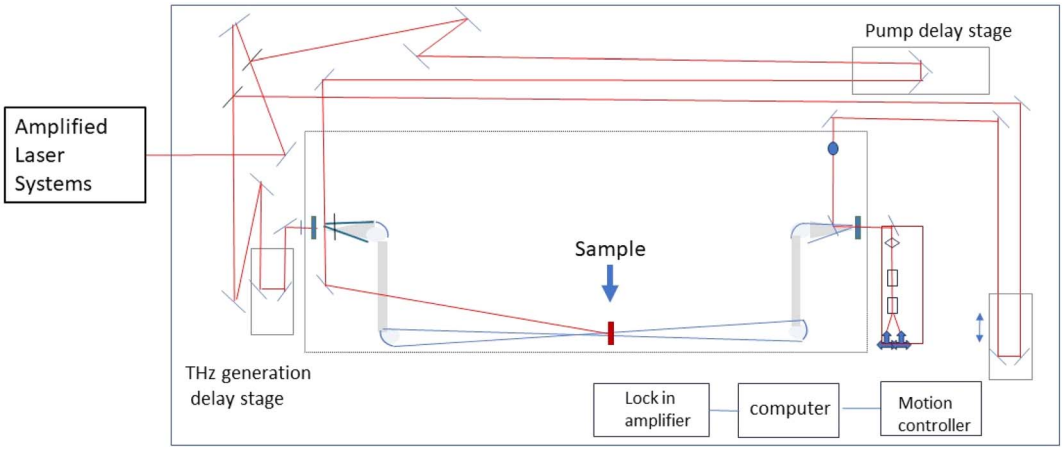

Fig. 1 THz-TDS and TRTS setup utilized for the measurements.

third beam is used for the photoexcitation of the sample with 800 nm (1.55 eV, 0.5 mJ). A non-linear crystal, beta-barium borate, is utilized for generation of 400 nm (3.10 eV, 0.025 mJ) pump excitation color from 800 nm. All experiments are carried out in a dry air environment with humidity less than 1%.

The software used to execute the DFT simulations is the Quantum Atomistic ToolKit (ATK) package.[42–44] All the calculations are performed in two steps. The first one regards the optimization of the geometries in both the single crystals, and, the interfaces of the layered hybrid structures. The structures that have been geometrically relaxed are then used for the calculation of the electronic and optical properties as the second step. To perform the entire cycle of analyses, the energy cut-off is set at 1200 eV and the Brillouin-zone integration is used a $15 \times 15 \times 15$ k-points grid, in order to have a total energy convergence of 5.0×10^{-6} eV per atom, a maximum stress of 2.0×10^{-2} GPa, and a maximum displacement of 5.0×10^{-4} Å. For the DFT calculations, the electron basis uses a linear combination of the atomic orbital (LCAO) associated with the Perdew–Burke–Ernzerhof (PBE) generalized gradient approximation (GGA) density functional for the electron exchange-correlation energy.[45] For each atom, the ionic cores are represented by norm-conserving (NC) PseudoDojo (PDj) pseudopotentials, and the dispersion correction Grimme DFT-D3 term is used to better describe the van der Waals interactions between the layers, which are not adequately predicted by standard DFT functionals.[46] Due to the layered nature of the samples under test, the periodic boundary conditions (PBCs) are applied only to the a and b axes in order to maintain a high level of accuracy, to avoid problems with boundary effects caused by the finite size, and to get a reasonable calculation time. The optical properties have been determined by two components of the dielectric function $\varepsilon(\omega)$ that are $\varepsilon_{\mathrm{real}}(\omega)$ and $\mathrm{i}\varepsilon_{\mathrm{im}}(\omega)$. The imaginary part $\varepsilon_{\mathrm{im}}(\omega)$ of the dielectric constant can be determined from eqn (1):[47]

$$\varepsilon_{\mathrm{im}}(\omega) = \frac{4\pi^2}{\Omega\omega^2} \sum_{i\in \mathrm{HOMO}, j\in \mathrm{LUMO}} \sum_k W_k \left|\rho_{ij}\right|^2 \delta\left(\varepsilon_{kj} - \varepsilon_{ki} - \hbar\omega\right) \quad (1)$$

where HOMO, LUMO, ω, Ω, W_k, ρ_{ij} were the valence band, conduction band, photon frequency, volume of the lattice, weight of the k-point, and elements of the dipole transition matrix, respectively.

The real part of the dielectric constant can be obtained with the following eqn (2):[47]

$$\varepsilon_{\mathrm{real}}(\omega) = 1 + \frac{1}{\pi} P \int_0^\infty \mathrm{d}\overline{\omega} \frac{\overline{\omega}\varepsilon_2(\overline{\omega})}{\overline{\omega}^2 - \omega^2} \quad (2)$$

Finally, the refractive index (n) and extinction coefficient (k) of the systems have been calculated as in eqn (3) and (4):

$$\varepsilon_{\mathrm{real}}(\omega) = n^2 - k^2 \quad (3)$$

$$\varepsilon_{\mathrm{im}}(\omega) = 2nk \quad (4)$$

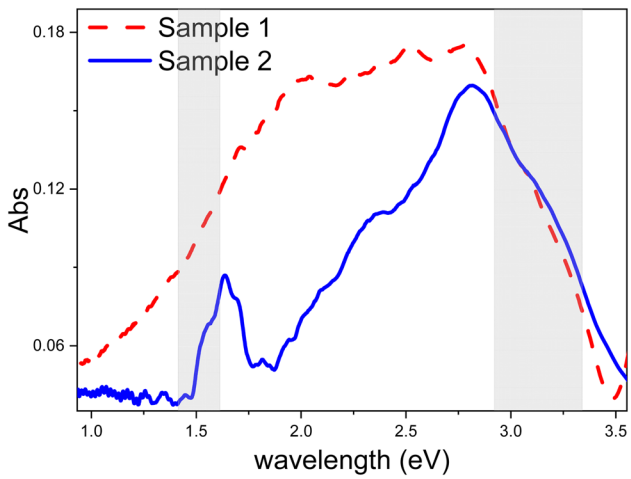

Fig. 2 UV-Vis spectra of Sample 1 (1L $MoSe_2$ + 2L $PtSe_2$) (dashed red line) and Sample 2 (3L WSe_2) (solid blue line). The gray areas represent the excitation wavelengths of 800 nm (1.55 eV) and 400 nm (3.10 eV) with their corresponding bandwidths for TRTS studies.

Open Access Article. Published on 02 January 2026. Downloaded on 1/21/2026 12:58:23 AM.
This article is licensed under a Creative Commons Attribution-NonCommercial 3.0 Unported Licence.

Results and discussions

Fig. 2 presents the UV-Vis spectra of the samples. Sample 1 consisting of 1L $MoSe_2$ + 2L $PtSe_2$ on mica exhibits a broad absorption feature spanning 1.5–3.25 eV. The broad absorption appears as two shoulders at 1.88 eV and 2.85 eV, superimposed on a main band at 2.26 eV (red-dashed line in Fig. 2). A direct bandgap of *ca.* 1.42 eV and an indirect bandgap of *ca.* 1.23 eV are estimated for Sample 1 from the tauc plots. In their study, Mondal *et al.* presented nonlinear optical susceptibility and THz conductivity of multilayer $MoSe_2$ and multilayer $MoSe_2$ on Pt NPs. While the bare $MoSe_2$ sample showed a bandgap of 1.50 eV, the $MoSe_2$ + Pt NPs sample resulted in a bandgap of 1.39 eV, showing that the addition of Pt nanoparticles lowered the bandgap.[48] In another study by Zhao *et al.* on electron mobility properties of $PtSe_2$ the bandgap was tuned from 1.13 eV for 1L $PtSe_2$ to zero for 100 nm thin film.[23] The studies showed that the bandgap of such 2D materials is highly affected by the number of layers and the interacting vdW materials. Therefore, this reduction in bandgap to 1.42 eV is attributed to combined multilayer structure and interlayer vdW interactions, consistent with the literature. In addition, the indirect bandgap of *ca.* 1.23 eV may correspond to the double layer $PtSe_2$, since 1L $MoSe_2$ does not show an indirect bandgap as discussed in the theoretical part.

Fig. 2 also presents the UV-Vis spectra of Sample 2, consisting of 3L WSe_2 on mica. Sample 2 exhibits a distinct absorption peak at nearly 1.6 eV, and a broader absorption feature centered at 2.8 eV, accompanied by shoulders at 2.3 eV and 3.2 eV (blue-solid line in Fig. 2). A direct bandgap of ~1.47 eV is observed for Sample 2, with no indirect transition. In their study, Liu *et al.* reported an absorption band centered at 1.64 eV for a monolayer WSe_2.[49] This may be a characteristic absorption of WSe_2 that persists in multilayer structures, supporting the behavior of Sample 2. Additionally, a study by Zhou *et al.* on the optical properties of WSe_2 layers demonstrated a comparable bandgap value of 1.44 eV.[50] These findings suggest that, although layer thickness influences the optical absorption of WSe_2, the primary spectral features of single layer are retained in multilayer structures. We believe this behavior is observed for Sample 2.

The structural purity and layer numbers are monitored also by Raman spectroscopy and the corresponding spectra are presented in Fig. 3. Sample 1 (1L $MoSe_2$ + 2L $PtSe_2$) shows two main Raman bands at 173 cm^{-1} and 233 cm^{-1}, along with a relatively weak and broad feature around 200 cm^{-1}. The bands located at 173 cm^{-1} and 200 cm^{-1} are attributed to $PtSe_2$ layers and corresponds to E_g and A_{1g} modes.[51] The band at 233 cm^{-1} is associated with the $MoSe_2$ monolayer.[52] These Raman features are in good agreement with the literature.[53] Fig. 3 also presents the Raman spectrum of Sample 2 (3L WSe_2). The main feature is observed at 243 cm^{-1} while a very weak and broad band is observed at 300 cm^{-1} (not shown). The bands correspond to the E_{2g} and B_{2g} modes of WSe_2, again consistent with the literature.[54]

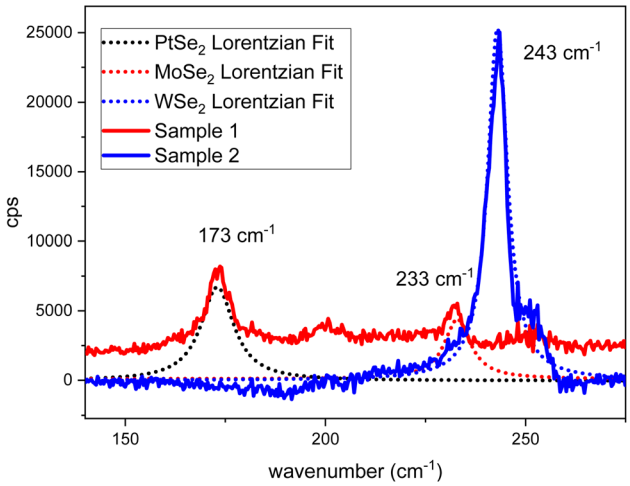

Fig. 3 Raman spectra of Sample 1 (1L $MoSe_2$ + 2L $PtSe_2$, red) and Sample 2 (3L WSe_2, blue) together with their Lorentzian fits (dotted lines). The spectra were background corrected with respect to the Mica reference. For $PtSe_2$, there is a second peak around 200 cm^{-1} that should also be considered in the fits, its intensity is weak in agreement with the 2L thickness of $PtSe_2$.[32]

Fig. 4a and b show the RHEED patterns of Sample 1 along the [100] crystal axis of $MoSe_2$ and $PtSe_2$ respectively. In the insets, the patterns along the [1$\bar{1}$0] crystal axis clearly demonstrate the single crystalline character of the layers. The intensity profiles in Fig. 4c also prove the weak vdW interaction between the two TMDC layers, each layer displaying its own lattice parameter. Fig. 4d and e are illustrating the van der Waals stacking and the epitaxial relationship between $MoSe_2$ and $PtSe_2$. The RHEED patterns of 1L, 2L and 3L of WSe_2 long [100] crystal axis are shown in Fig. 4f–h, respectively. All three patterns look very similar demonstrating the layer-by-layer growth of the film and they all exhibit a doublet (see white arrows in Fig. 4e) close to the second order diffraction position indicative of an isotropic character: some WSe_2 grains are randomly oriented in the film plane.

In Fig. 5, X-ray diffraction confirms these observations. The radial (Fig. 5a) and azimuthal (Fig. 5c) scans of Sample 1 display a clear anisotropic character confirming the single crystalline character of the film. We only observe a weak mosaic spread of 2–3° reflecting the slight in-plane misorientation of $MoSe_2$/$PtSe_2$ grains. However, for Sample 2, the same WSe_2 Bragg peaks are observed along the three different azimuths in radial scans (Fig. 5b), and 56% to 71% (orange areas in Fig. 5d) of WSe_2 are randomly oriented in the film plane. Moreover, the mosaic spread (≈7°) is twice larger than the one of Sample 1. Finally, the morphology of Sample 1 and Sample 2 is investigated by atomic force microscopy (AFM) and presented in Fig. 6. They both show full coverage. In Fig. 6a, the brightest grains correspond to the starting growth of the 3rd $PtSe_2$ layer and in Fig. 6b, we clearly see the 3rd WSe_2 layer almost completed.

The atomistic theoretical characterization of $PtSe_2$, $MoSe_2$, and WSe_2 as individual entities, is the initial step to understand the properties of the systems based on the layered hybrid structures. $PtSe_2$, $MoSe_2$, and WSe_2 TMDC are materials built in

 © 2026 The Author(s). Published by the Royal Society of Chemistry

Open Access Article. Published on 02 January 2026. Downloaded on 1/21/2026 12:58:23 AM.
This article is licensed under a Creative Commons Attribution-NonCommercial 3.0 Unported Licence.

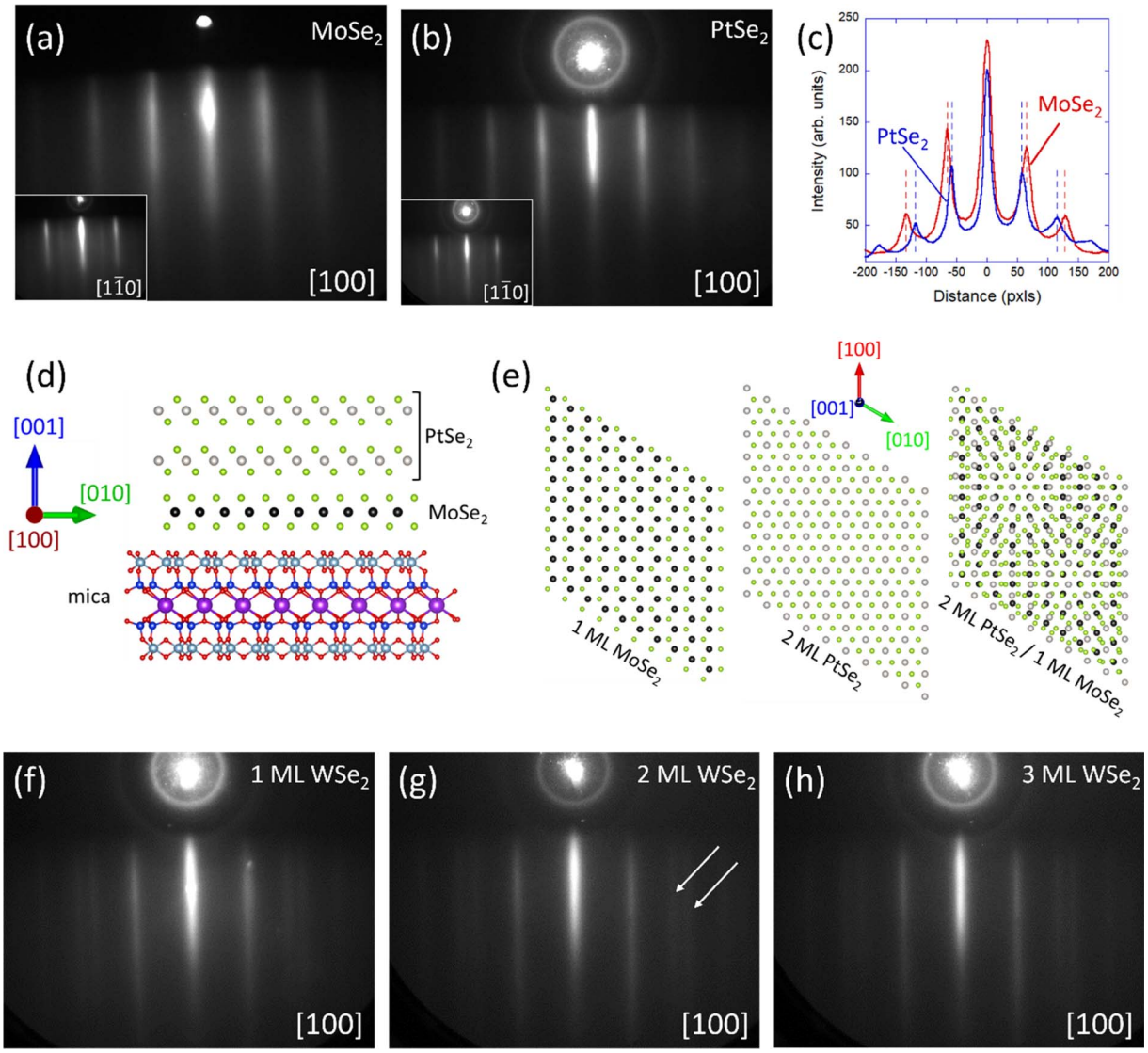

Fig. 4 (a) and (b) RHEED patterns along [100] of (a) 1L $MoSe_2$ epitaxially grown on mica and (b) 2L $PtSe_2$ epitaxially grown on $MoSe_2$. Insets are showing the RHEED patterns along [1$\bar{1}$0]. (c) Intensity profiles of RHEED patterns of $MoSe_2$ (in red, from (a)) and $PtSe_2$ (in blue, from (b)). (d) and (e) Schematic side and top view of the $PtSe_2$ (2L)/$MoSe_2$ (1L) stacking showing the epitaxial relationship. (f–h) RHEED patterns along [100] of 1L, 2L and 3L of WSe_2 epitaxially grown on mica, respectively.

a layered structure where the layers are stacked together by vdW interactions while the atoms are covalently bonded in the plane; all the considered materials are in their hexagonal (H) configuration. The properties of the 2D monolayers of $PtSe_2$, $MoSe_2$, and WSe_2 are considered since they exhibit distinct electronic structures and optical properties compared to their respective bulk material. For each single crystal, the projected density of the states (PDOS) and band structure have been evaluated to understand and verify the reliability of the proposed DFT methodology.

1L of $PtSe_2$ is characterized by a hexagonal crystal structure in which a central line of Pt atoms is covalently linked to a sheet of Se atoms above and below (Fig. 7a). Its band structure originates an indirect band gap of 1.36 eV and a direct bandgap of 1.57 eV that is in good agreement with the observed experimental result (1.23 eV for indirect and 1.42 eV for direct bandgap of Sample 1) and with the literature.[55] The presence of the gap between the valence and the conduction bands that originated from both the Pt and Se contributions is even confirmed in the PDOS (Fig. 7b and c). The PDOS contribution arises from the d-orbital energy level of Pt and the p-orbitals energy level of Se and both contribute to the valence and the conduction bands. $MoSe_2$, schematically represented in Fig. 7d in its monolayer form, is a direct bandgap semiconductor, the maximum of the valence band and the minimum of the conduction band occur at the *K*-point in the Brillouin zone. The bandgap calculated for 1L $MoSe_2$ is 1.56 eV (Fig. 7e), which is in line with the observed experimental bandgap (1.42 eV of Sample 1, shift is due to the combination structure) and with the reported in literature.[56] Both the elements, Mo and Se,

Open Access Article. Published on 02 January 2026. Downloaded on 1/21/2026 12:58:23 AM.
This article is licensed under a Creative Commons Attribution-NonCommercial 3.0 Unported Licence.

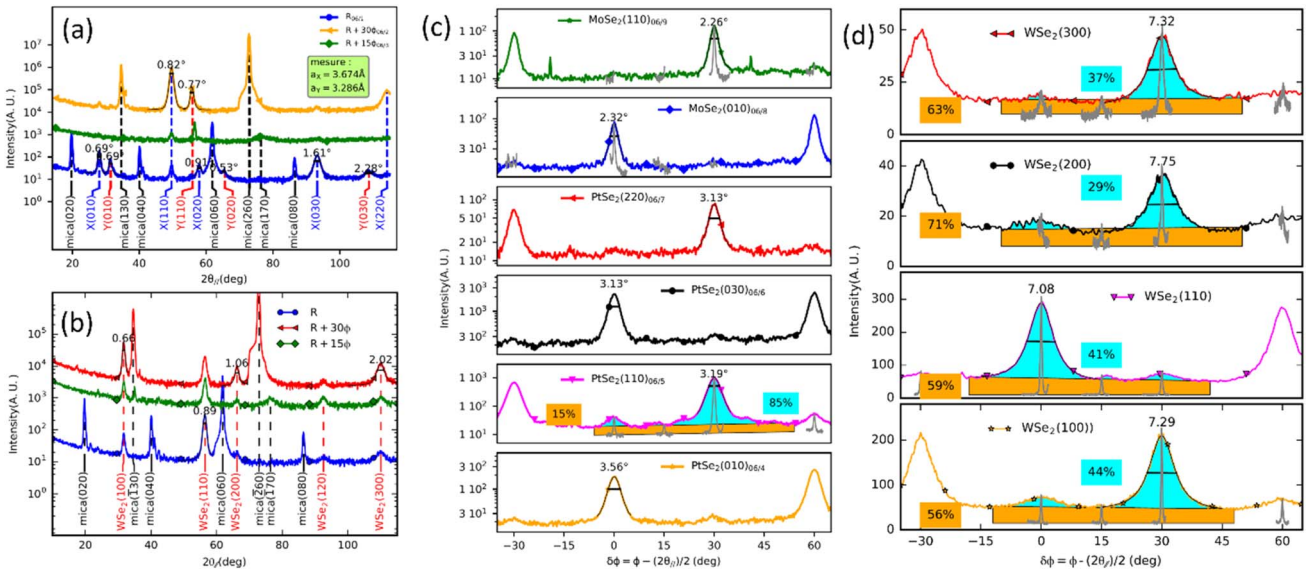

Fig. 5 X-ray diffraction spectra. (a) and (b) Radial scans along 3 different in-plane azimuths of Sample 1 (1L $MoSe_2$ + 2L $PtSe_2$) and Sample 2 (3L WSe_2) respectively. In (a), *X* phase corresponds to $PtSe_2$ and *Y* phase to $MoSe_2$ respectively. (c) and (d) Azimuthal scans for different Bragg peaks of $MoSe_2$ and $PtSe_2$ of Sample 1 and WSe_2 of Sample 2 respectively. The numbers in degrees above each Bragg peak correspond to their full width at half maximum. The numbers in % in orange and blue correspond to the fraction of isotropic and anisotropic crystal grains respectively.

contributed to the valence and the conduction bands in the PDOS as observed in 1L $PtSe_2$ (Fig. 7f). In addition, the broad energy distribution of the DOS with high structure observed for both TMDCs confirms the broad absorption with multiband nature in the UV-Vis spectrum where Sample 1 has a strong band centered around 2.3 eV.

The band structure of WSe_2 moves from an indirect to direct bandgap when passing from bulk to a single layer. Similarly to the $MoSe_2$, the monolayer of WSe_2 is characterized by a direct band gap of 1.68 eV originated from a valence band maximum and conduction band minimum both at the *K*-point, while the bulk material has an indirect band gap of 0.94 eV.[41] Similar to other 1L TMDCs, the PDOS contribution also arises from the d-orbitals energy level of W atoms and the p-orbitals energy level of Se and both contributed the valence and the conduction bands.

Sample 1, based on the layered structures 1L $MoSe_2$ + 2L $PtSe_2$ (Fig. 8a), was created, and the interface between the two materials was geometrically relaxed. The interface is created by stacking together the layered (1L $MoSe_2$ + 2L $PtSe_2$) structures in the "*c*" direction. It is evident that the Se contribution leads to a closure of the band gap; as noted from the PDOS of Sample 1 (Fig. 8b). Here, the Se orbitals cross the Fermi level, being the main contributors to the valence and conduction edges. It is also important to note that beyond the effect of Se, the valence band edge is influenced by contributions from both Mo and Pt, while Pt plays a more decisive role in the conduction part of the PDOS. Furthermore, the refractive index (n) and extinction coefficient (k) were evaluated across the spectral range of 0 to 1.5 THz. Both optical parameters remain nearly constant throughout the entire frequency range examined. For Sample 1, the refractive index is calculated to be 2, while the extinction coefficient is almost 0. The estimations are consistent with the observed terahertz behavior.

Sample 2 (3L WSe_2, stacked in the "*c*" direction) is schematically illustrated in Fig. 9a. In this instance, the differences

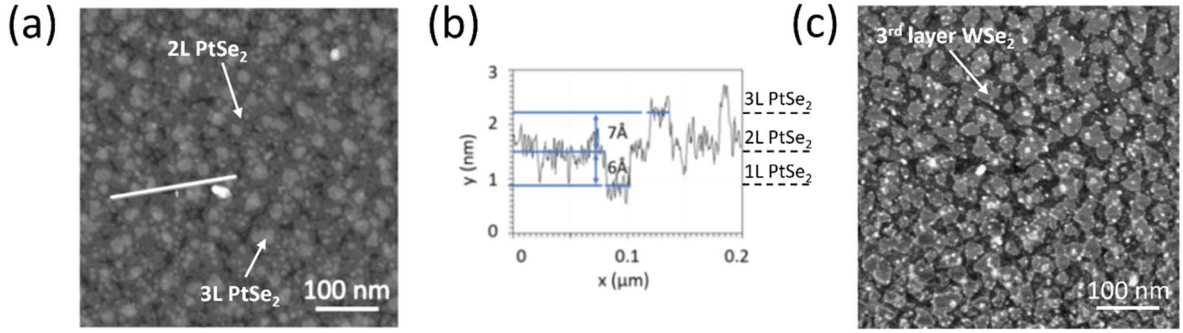

Fig. 6 (a) 500 × 500 nm^2 AFM image of Sample 1 (1L $MoSe_2$ + 2L $PtSe_2$) showing almost 100% coverage. (b) Height profile recorded along the white line in (a) showing the vdW stacking. (c) 500 × 500 nm^2 AFM image of Sample 2 (3L WSe_2).

 © 2026 The Author(s). Published by the Royal Society of Chemistry

Open Access Article. Published on 02 January 2026. Downloaded on 1/21/2026 12:58:23 AM.
This article is licensed under a Creative Commons Attribution-NonCommercial 3.0 Unported Licence.

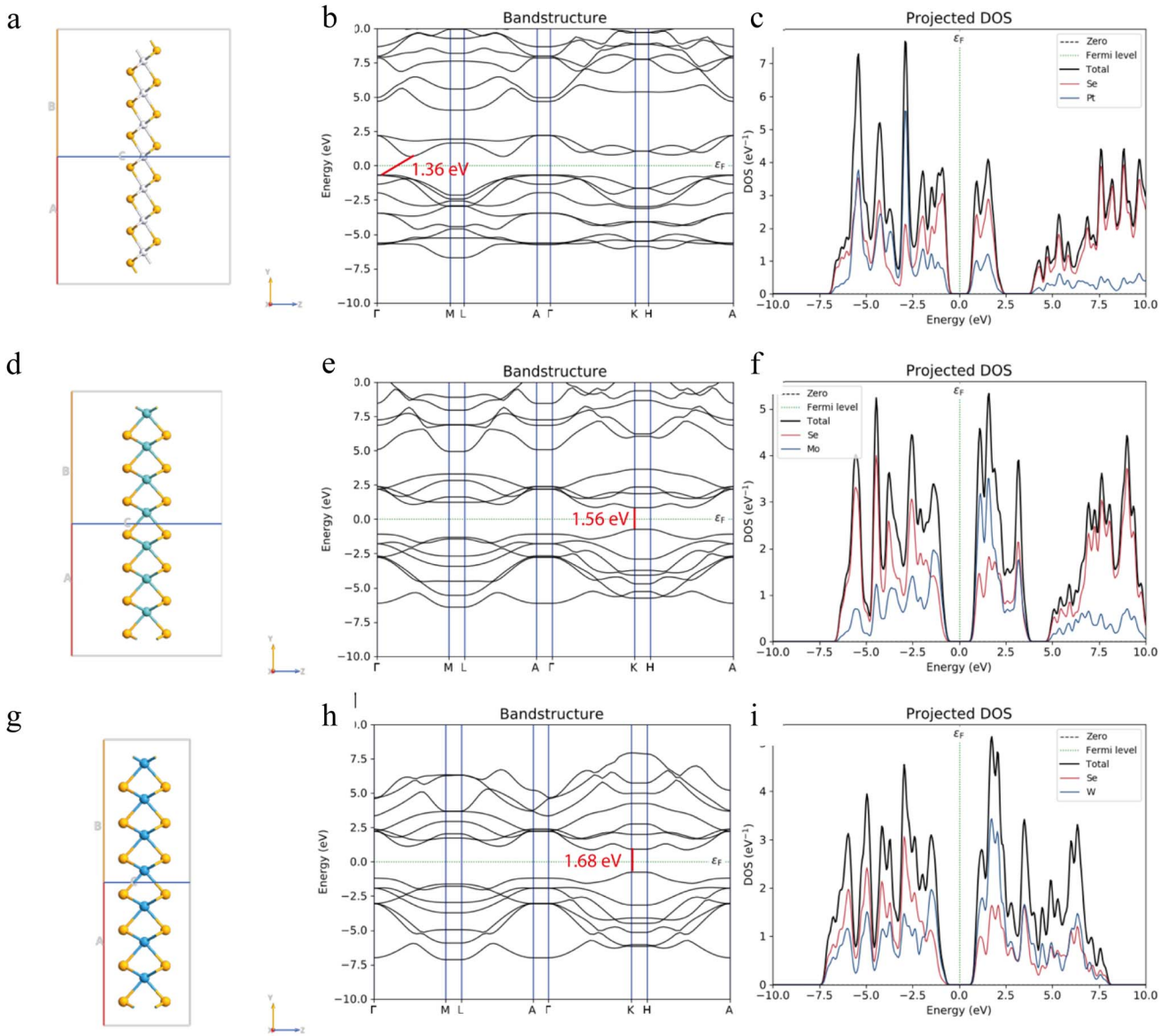

Fig. 7 Electronic properties of $PtSe_2$, $MoSe_2$, and WSe_2 as single layer. (a) Schematic representation of $PtSe_2$, (b) its respective bandstructure, and (c) its PDOS. (d) Molecular structure of $MoSe_2$, (e) its respective bandstructure and (f) its PDOS. (g) Atomistic arrangement of WSe_2, (h) its respective bandstructure, and (i) its PDOS.

with the 1L are less pronounced compared to Sample 1, most probably because the material is not a hybrid system. Indeed, the most noticeable impact is a slight reduction in the band gap, as seen from the diminution of the distance between the valence and the conduction portion of the PDOS; this is not unexpected, as it is well known that WSe_2 has a transition from a direct to an indirect band gap, with values shifting from 1.68 eV in the single layer to 0.94 eV in the bulk system. The calculated direct bandgap is consistent with the experimental observation of a direct bandgap only at *ca.* 1.47 eV. Similar to Sample 1, the refractive index and extinction coefficient for Sample 2 were assessed in the frequency range from 0 to 1.5 THz. Both optical parameters remain also almost flat within the entire considered frequency range. The refractive index is determined to be 2, while the extinction coefficient is close to 0.

Fig. 10a and b present the THz time–domain profiles and corresponding frequency-domain spectra of the air reference and Sample 1. Sample 1 consists of a 170 μm thick mica substrate, with 1L of $MoSe_2$ and 2L of $PtSe_2$ sequentially deposited on top. The mica shows about 85% transmission of the THz light for this thickness. The observed transmission loss is attributed to insertion losses at the mica–air interfaces, caused by the refractive index mismatch. The THz spectrum of the air reference shows the spectral bandwidth of the instrument up to almost 3 THz, which reduces to 2.5 THz bandwidth due to the mica substrate of Sample 1. No significant additional loss is observed from the 2D layers, consistent with theoretical calculations indicating an almost zero extinction coefficient (k). The observed fringes on mica (not shown) and Sample 1 arise

Open Access Article. Published on 02 January 2026. Downloaded on 1/21/2026 12:58:23 AM.
This article is licensed under a Creative Commons Attribution-NonCommercial 3.0 Unported Licence.

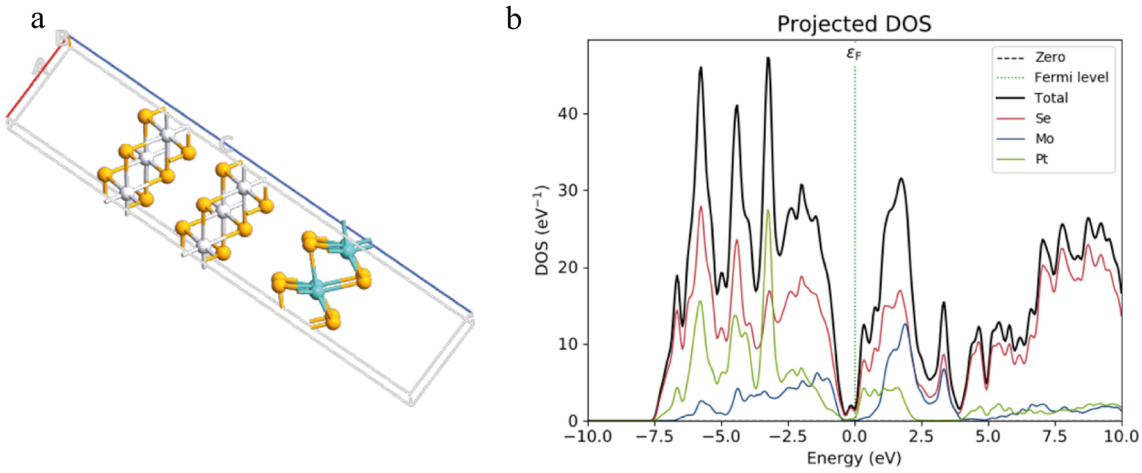

Fig. 8 (a) Schematic representation of the unit cell of the Sample 1 and (b) its respective PDOS.

from internal THz reflections within the substrate, manifesting in the time–domain profiles around 3.5 ps and 5 ps.

Sample 2, in contrast, consists of a 90 μm thick mica substrate with 3L of WSe_2 deposited on top. Fig. 10c and d similarly present the THz time–domain profiles and corresponding frequency–domain spectra of air reference and Sample 2. As in Sample 1, the observed signal attenuation arises from insertion loss at the air–mica interfaces. On the other hand, the secondary reflection pulse, appearing around 2.5 ps, is observed earlier than in Sample 1 due to the thinner mica substrate. The spectral bandwidth is also around 2.5 THz and no significant additional loss is observed due to the 2D layers, consistent with their low absorption in the THz range.

Fig. 11 presents the refractive index (n) and extinction coefficient (k) of the mica substrate, as well as the effective n and k of Sample 1 and Sample 2. The mica shows minimal absorption of THz radiation (almost zero extinction coefficient) as expected. In addition, the TMDC layers of Sample 1 and Sample 2 do not introduce any observable absorption as simulated in the theoretical calculations. Thus, effective k is also almost zero similar to the bare mica response. Due to substrate thickness differences between the mica reference and the samples, low signal-to-noise ratios, and nanometer thickness of the TMDC layers, it is not feasible to directly extract the intrinsic TMDC dielectric properties. Nevertheless, the findings are significant for applications involving terahertz radiation, such as medical imaging or security screening. A noticeable increase in effective refractive index is observed for both Sample 1 and Sample 2 relative to the bare mica substrate. Even a few layers of 2D materials significantly affect the effective refractive index of the materials. Mica has an average refractive index of *ca.* 2.5, and its refractive index remains almost constant in the 0.1–1.4 THz range. Sample 1 also exhibits a nearly flat refractive index spectrum as suggested by the theoretical study, with an effective index of *ca.*

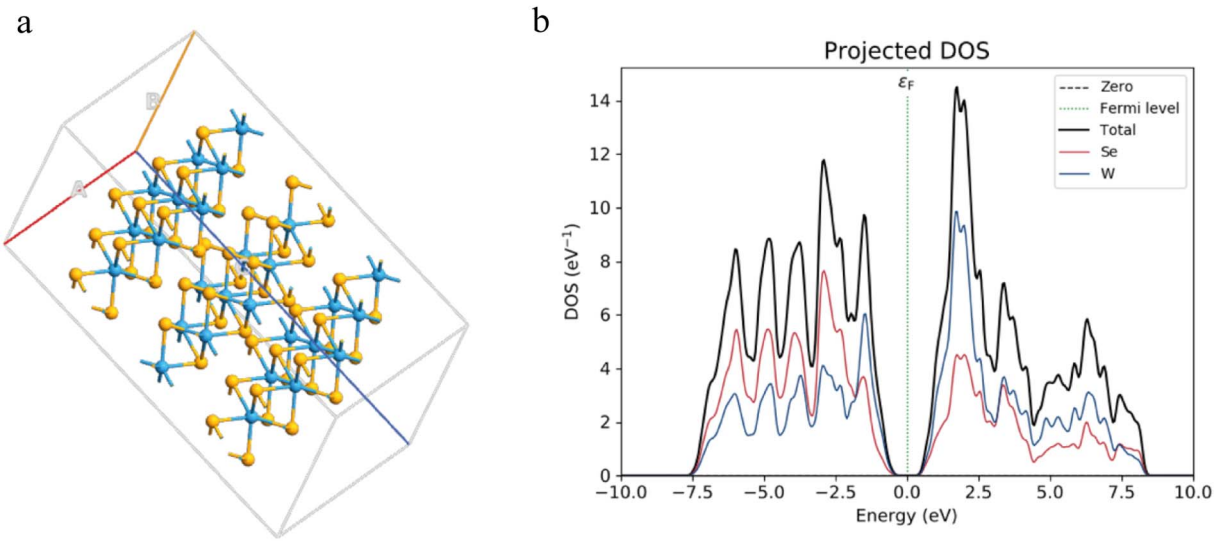

Fig. 9 (a) Schematic representation of the unit cell of 3L WSe_2 (Sample 2) and (b) its PDOS.

 © 2026 The Author(s). Published by the Royal Society of Chemistry

Open Access Article. Published on 02 January 2026. Downloaded on 1/21/2026 12:58:23 AM.
This article is licensed under a Creative Commons Attribution-NonCommercial 3.0 Unported Licence.

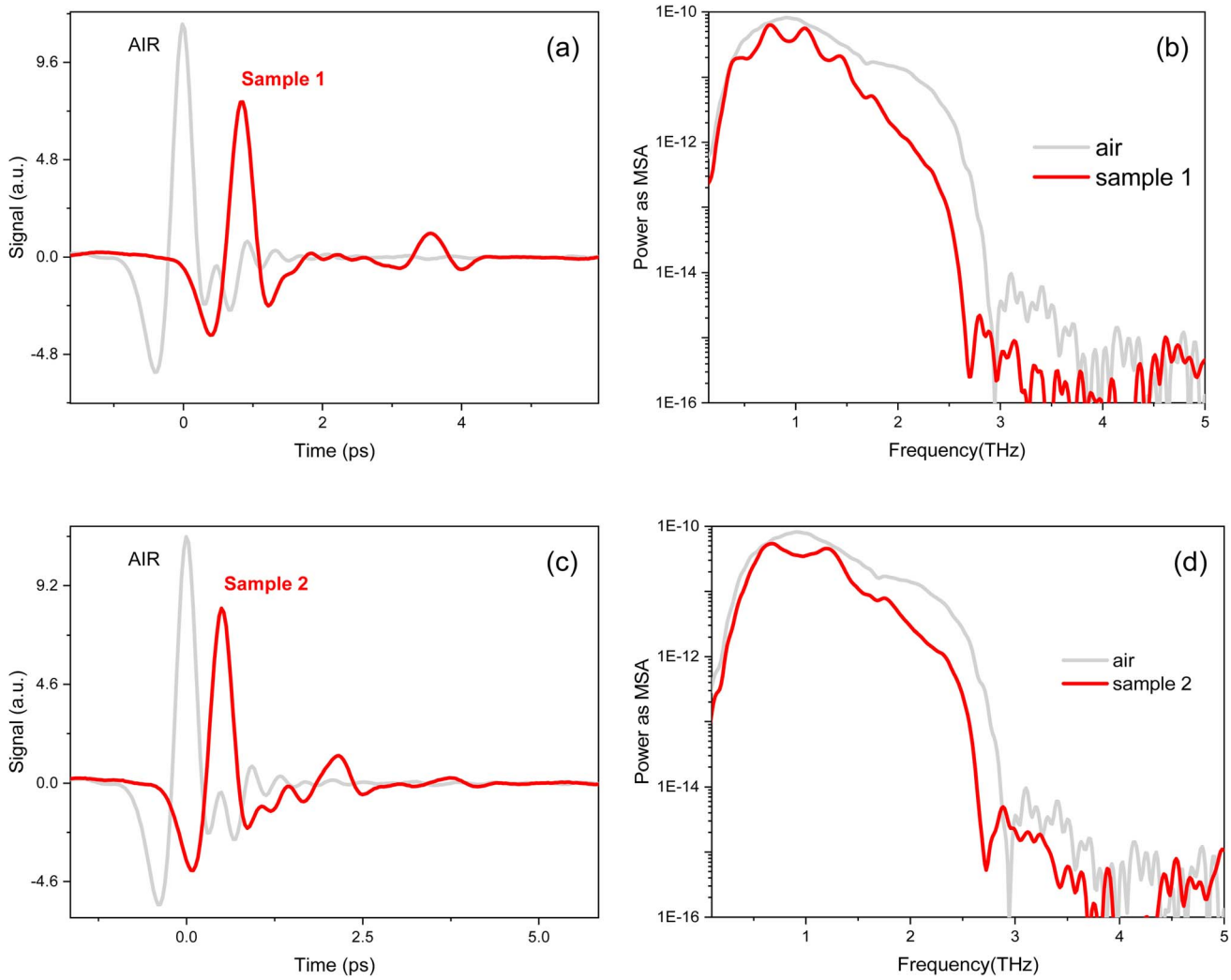

Fig. 10 (a) THz time–domain profiles and (b) corresponding frequency-domain spectra of air reference and Sample 1 (1L $MoSe_2$ + 2L $PtSe_2$) and (c) THz time–domain profiles and (d) corresponding frequency domain spectra of reference air and Sample 2 (3L WSe_2).

2.7 in the same frequency range. Similarly, Sample 2 also displays a nearly featureless and flat refractive index with an average refractive index of 2.7 in the same frequency range. These behaviors highlight the potential of 2D materials for broadband THz applications.

Fig. 12 shows the differential THz transmission data of the samples collected with the TRTS system. The samples are photoexcited using 400 nm and 800 nm pulses with fluences of 195 μJ cm^{-2} and 225 μJ cm^{-2}, respectively, and probed by broadband THz light. TRTS measures changes in THz

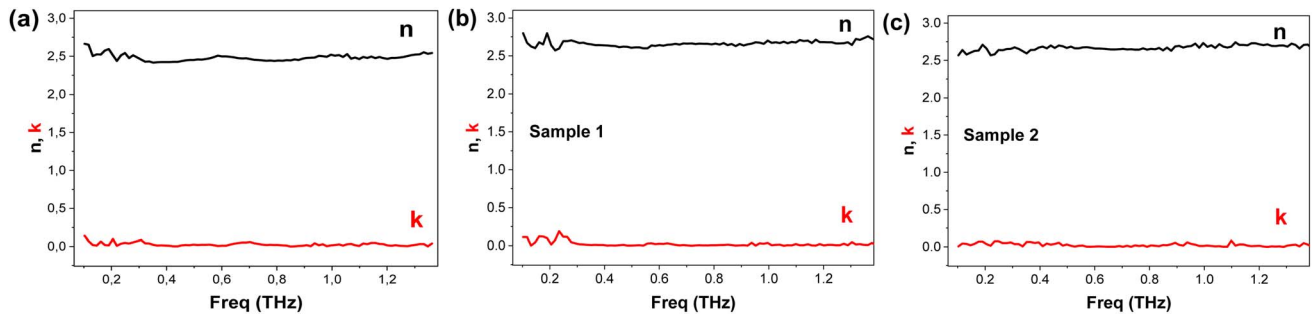

Fig. 11 Refractive index (*n*) and extinction coefficient (*k*) of (a) mica substrate and (b) Sample 1 (mica + 1L $MoSe_2$ + 2L $PtSe_2$), (c) Sample 2 (mica + 3L WSe_2).

Open Access Article. Published on 02 January 2026. Downloaded on 1/21/2026 12:58:23 AM.
This article is licensed under a Creative Commons Attribution-NonCommercial 3.0 Unported Licence.

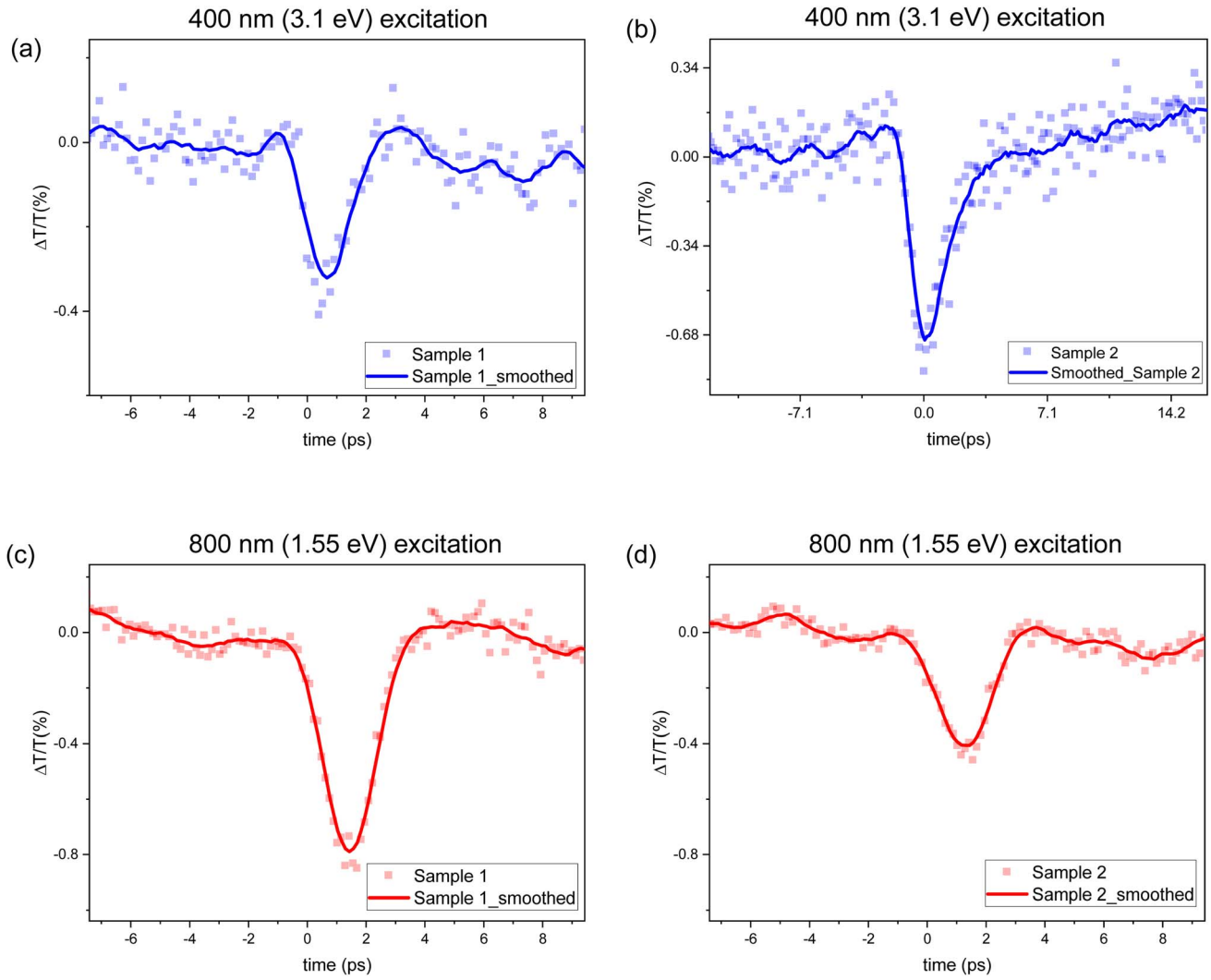

Fig. 12 Differential THz transmission, $\Delta T/T_0$, of (a) Sample 1 and (b) Sample 2 as a function of pump–probe delay recorded at a fluence of 195 μJ cm^{-2} for 400 nm excitation and $\Delta T/T_0$ of (c) Sample 1 and (d) Sample 2 at a fluence of 255 μJ cm^{-2} for 800 nm excitation. (The solid lines are 20-point Savitzky–Golay averaging).

transmission as a function of the delay between the optical pump and the THz probe, providing a direct insight into the intrinsic carrier dynamics of the material. Unfortunately, the differential transmission signals obtained under 400 nm excitation were notably noisy, attributed to weak photoconductive response. When Sample 1 is excited with 400 nm light (above the band gap, Fig. 12a), it initially exhibits a fast response with a rise time of ∼1 ps, followed by a similar decay time. On the other hand, under 800 nm excitation (Fig. 12c), Sample 1 displays a faster rise time of ∼0.36 ps—potentially limited by the system's time resolution— and a decay time comparable to the 400 nm case (∼1 ps). Compared to 400 nm excitation, the observed photoconductivity under 800 nm excitation is significantly higher.

Fig. 12b and d show the THz carrier dynamics of Sample 2 upon photoexcitation with ultrafast 400 nm and 800 nm, using the same fluences as for Sample 1. The response of Sample 2 is stronger than that of Sample 1 under 400 nm excitation, but significantly weaker under 800 nm excitation. In this case, a 400 nm optical excitation of Sample 2 results in a faster response, with a rise time of approximately 0.45 ps. A slower decay is also observed, indicating a longer average carrier lifetime. Under 800 nm excitation, Sample 2 exhibits a rapid rise time of ∼1 ps and fall time of ∼0.7 ps. The longer-lived photocarriers in Sample 2 must be related to the difference in electronic structure. With a complex electronic band structure due to the hybrid character, Sample 1 possesses more radiative or non-radiative channels than Sample 2 for carrier relaxation.

The measurements closely align with the reported study by Docherty *et al.*[37] on similar 2D materials, where an initial sharp rise and a fast decay with a relatively short carrier lifetime were observed. However, due to the low signal-to-noise ratios, it is not possible to accurately extract carrier mobilities and concentrations from these data. Although, the absorption of Sample 2 near 400 nm (3.1 eV, indicated by gray area) is similar to that of Sample 1, both being above the bandgap excitations-, Sample 2

 © 2026 The Author(s). Published by the Royal Society of Chemistry

Open Access Article. Published on 02 January 2026. Downloaded on 1/21/2026 12:58:23 AM.
This article is licensed under a Creative Commons Attribution-NonCommercial 3.0 Unported Licence.

exhibits a stronger THz response, indicating higher photoconductivity. Analysis of the PDOS suggests that this difference may primarily arise from the higher DOS of W near the valence band and conduction edges, compared to Mo and Pt. In Sample 1, excitations at 3.1 eV (400 nm) likely induce transitions such as Se-to-Se and Mo-to-Se, whereas transitions involving Se-to-Mo are less probable. In Sample 2, the 3.1 eV excitations result in transitions most likely from Se-to-W or W-to-Se and less likely from Se to Se. Therefore, the greater number of photoexcited electrons transferred to the W network in Sample 2 may explain the observed long carrier lifetime.

The differential transmission spectra upon excitation with 800 nm (1.55 eV) presented in Fig. 12c and d show a stronger THz response for Sample 1 compared to Sample 2. There are two main reasons why Sample 1 exhibit a stronger response under 800 nm excitation. Firstly, the 1.55 eV excitation is above the bandgap of Sample 1 (1.23 eV) while it is around the bandgap of Sample 2 (1.47 eV). The excitation laser pulse is ultrashort and hence very broad (gray region around 1.5 eV in Fig. 2). This enables partial overlap with the bandgap. Secondly, the absorption of Sample 1 is around twice that of Sample 2. Hence, it has a greater probability of carrier generation. Despite its weaker absorption and less favorable excitation energy alignment, Sample 2 still demonstrates significant carrier generation and dynamics, confirming its higher photoconductivity compared to Sample 1. The results show that WSe_2 is a very promising candidate for high-speed electronic applications with its fast rise and fall time responses and significantly higher photoconductivity.

Conclusion

In conclusion, our combined time-resolved measurements and density functional analysis reveal distinct photoconductive behaviors of the two TMDC structures. Sample 2, consisting of 3L WSe_2 on mica substrate, exhibits higher photoconductivity under 400 nm excitation. The PDOS investigation showed that this is primarily due to having a higher density of W-dominated states near the valence band edge, in contrast to Sample 1, where the corresponding states are predominantly Se-derived. As a result, dominant optical transitions in Sample 2 occur between Se and W atoms. In contrast, Sample 1 with its 1L $MoSe_2$ and 2L $PtSe_2$ on mica shows transitions mainly from Se-to-Se and Mo-to-Se, and, to a lesser extent, Se-to-Mo, which contributes to a reduced photoconductive response under 400 nm excitation. The long-lived carrier response of Sample 2 is due to its electronic structure.

Under 800 nm excitation, Sample 1 displays better THz response since the excitation energy (1.55 eV) lies above its bandgap coincides with high density of states, as shown in PDOS with stronger absorbance. Although Sample 2 exhibits a weaker absorption and a lower density of available states at this energy, it still shows a significant response, confirming superior conductivity of the WSe_2 structure.

These findings demonstrate that the conductivity of TMDC structures is highly sensitive to the elemental composition and stacking configuration that govern the resulting electronic band structure. This study highlights the potential of tailoring TMDC structures for ultrafast, wavelength-specific optoelectronic and terahertz applications.

Author contributions

M. Jamet, D. Mencarelli, O. Esenturk and H. Altan contributed to the conceptualization of the study, acquisition of funding, provision of resources, supervision, and preparation of the manuscript. C. Vergnaud, R. Sharma, A. Marty, E. Pavoni, E. Mohebbi, E. Laudadio and Y. S. Aytekin contributed to data curation, formal analysis and manuscript writing. C. Vergnaud, R. Sharma, A. Marty and M. Jamet performed the growth of the 2D materials and their structural characterization. E. Pavoni, E. Mohebbi, E. Laudadio and D. Mencarelli conducted the theoretical calculations and corresponding analysis. Y. S. Aytekin, O. Esenturk and H. Altan carried out the terahertz measurements and data analysis.

Conflicts of interest

The authors declare no conflict of interest.

Data availability

The data that support the findings of this study are available on request from the corresponding authors J. M., D. M., H. A., and O. E.

Acknowledgements

We would like to thank PLASNANO project (101099552) funded by European commission under the program of Horizon EIC Pathfinder Open 2022. We would also like to thank Prof. Dr. Alpan Bek and Batuhan Balkan for the Raman measurements, and thank to Turkish Accelerator and Radiation Laboratory (TARLA) for allowing us to use their ultrafast laser-amplifier system and infrastructures for this work, and Prof. Dr. Halime Gül Yağlıoğlu and Fatime Gülşah Akça for their kind help on amplified laser system.

References

1 Z. Wang, P. Zhou, Z. Li, X. Xia, R. Zhang, J. Chen and W. Hong, A Compact SiGe Amplifier-Frequency-Doubler Chain With 7.1-DBm P Sat and 98-GHz Bandwidth for Sub-THz Applications, *IEEE Trans. Microw. Theor. Tech.*, 2024, **72**(6), 3485–3495, DOI: 10.1109/TMTT.2023.3328031.

2 B. M. Heffernan, Y. Kawamoto, K. Maekawa, J. Greenberg, R. Amin, T. Hori, T. Tanigawa, T. Nagatsuma and A. Rolland, 60 Gbps Real-Time Wireless Communications at 300 GHz Carrier Using a Kerr Microcomb-Based Source, *APL Photonics*, 2023, **8**(6), 066106, DOI: 10.1063/5.0146957.

3 A. M. Elbir, K. V. Mishra, S. Chatzinotas and M. Bennis, Terahertz-Band Integrated Sensing and Communications: Challenges and Opportunities, *IEEE Aero. Electron. Syst. Mag.*, 2024, **39**(12), 38–49, DOI: 10.1109/MAES.2024.3476228.

Open Access Article. Published on 02 January 2026. Downloaded on 1/21/2026 12:58:23 AM.
This article is licensed under a Creative Commons Attribution-NonCommercial 3.0 Unported Licence.

4 F. Bonaccorso, Z. Sun, T. Hasan and A. C. Ferrari, Graphene Photonics and Optoelectronics, *Nat. Photonics*, 2010, **4**(9), 611–622, DOI: 10.1038/nphoton.2010.186.
5 Q. Bao and K. P. Loh, Graphene Photonics, Plasmonics, and Broadband Optoelectronic Devices, *ACS Nano*, 2012, **6**(5), 3677–3694, DOI: 10.1021/nn300989g.
6 S. H. Lee, M. Choi, T.-T. Kim, S. Lee, M. Liu, X. Yin, H. K. Choi, S. S. Lee, C.-G. Choi, S.-Y. Choi, X. Zhang and B. Min, Switching Terahertz Waves with Gate-Controlled Active Graphene Metamaterials, *Nat. Mater.*, 2012, **11**(11), 936–941, DOI: 10.1038/nmat3433.
7 Z. Sun, A. Martinez and F. Wang, Optical Modulators with 2D Layered Materials, *Nat. Photonics*, 2016, **10**(4), 227–238, DOI: 10.1038/nphoton.2016.15.
8 M. M. Uddin, M. H. Kabir, M. A. Ali, M. M. Hossain, M. U. Khandaker, S. Mandal, A. Arifutzzaman and D. Jana, Graphene-like Emerging 2D Materials: Recent Progress, Challenges and Future Outlook, *RSC Adv.*, 2023, **13**(47), 33336–33375, DOI: 10.1039/D3RA04456D.
9 I. Meric, M. Y. Han, A. F. Young, B. Ozyilmaz, P. Kim and K. L. Shepard, Current Saturation in Zero-Bandgap, Top-Gated Graphene Field-Effect Transistors, *Nat. Nanotechnol.*, 2008, **3**(11), 654–659, DOI: 10.1038/nnano.2008.268.
10 R. Balog, B. Jørgensen, L. Nilsson, M. Andersen, E. Rienks, M. Bianchi, M. Fanetti, E. Lægsgaard, A. Baraldi, S. Lizzit, Z. Sljivancanin, F. Besenbacher, B. Hammer, T. G. Pedersen, P. Hofmann and L. Hornekær, Bandgap Opening in Graphene Induced by Patterned Hydrogen Adsorption, *Nat. Mater.*, 2010, **9**(4), 315–319, DOI: 10.1038/nmat2710.
11 Y. Zhang, T.-T. Tang, C. Girit, Z. Hao, M. C. Martin, A. Zettl, M. F. Crommie, Y. R. Shen and F. Wang, Direct Observation of a Widely Tunable Bandgap in Bilayer Graphene, *Nature*, 2009, **459**(7248), 820–823, DOI: 10.1038/nature08105.
12 F. Xia, D. B. Farmer, Y.-M. Lin and P. Avouris, Graphene Field-Effect Transistors with High On/Off Current Ratio and Large Transport Band Gap at Room Temperature, *Nano Lett.*, 2010, **10**(2), 715–718, DOI: 10.1021/nl9039636.
13 J. Wang, R. Zhao, M. Yang, Z. Liu and Z. Liu, Inverse Relationship between Carrier Mobility and Bandgap in Graphene, *J. Chem. Phys.*, 2013, **138**(8), 084701, DOI: 10.1063/1.4792142.
14 S. H. Mir, V. K. Yadav and J. K. Singh, Recent Advances in the Carrier Mobility of Two-Dimensional Materials: A Theoretical Perspective, *ACS Omega*, 2020, **5**(24), 14203–14211, DOI: 10.1021/acsomega.0c01676.
15 H. Zeng, G.-B. Liu, J. Dai, Y. Yan, B. Zhu, R. He, L. Xie, S. Xu, X. Chen, W. Yao and X. Cui, Optical Signature of Symmetry Variations and Spin-Valley Coupling in Atomically Thin Tungsten Dichalcogenides, *Sci. Rep.*, 2013, **3**(1), 1608, DOI: 10.1038/srep01608.
16 H. Li, G. Lu, Y. Wang, Z. Yin, C. Cong, Q. He, L. Wang, F. Ding, T. Yu and H. Zhang, Mechanical Exfoliation and Characterization of Single- and Few-Layer Nanosheets of WSe_2, TaS_2, and $TaSe_2$, *Small*, 2013, **9**(11), 1974–1981, DOI: 10.1002/smll.201202919.
17 Y.-H. Lee, L. Yu, H. Wang, W. Fang, X. Ling, Y. Shi, C.-T. Lin, J.-K. Huang, M.-T. Chang, C.-S. Chang, M. Dresselhaus, T. Palacios, L.-J. Li and J. Kong, Synthesis and Transfer of Single-Layer Transition Metal Disulfides on Diverse Surfaces, *Nano Lett.*, 2013, **13**(4), 1852–1857, DOI: 10.1021/nl400687n.
18 H. Terrones, F. López-Urías and M. Terrones, Novel Hetero-Layered Materials with Tunable Direct Band Gaps by Sandwiching Different Metal Disulfides and Diselenides, *Sci. Rep.*, 2013, **3**(1), 1549, DOI: 10.1038/srep01549.
19 A. Splendiani, L. Sun, Y. Zhang, T. Li, J. Kim, C.-Y. Chim, G. Galli and F. Wang, Emerging Photoluminescence in Monolayer MoS_2, *Nano Lett.*, 2010, **10**(4), 1271–1275, DOI: 10.1021/nl903868w.
20 X. Wang, Z. Song, W. Wen, H. Liu, J. Wu, C. Dang, M. Hossain, M. A. Iqbal and L. Xie, Potential 2D Materials with Phase Transitions: Structure, Synthesis, and Device Applications, *Adv. Mater.*, 2019, **31**(45), 1804682, DOI: 10.1002/adma.201804682.
21 V. K. Sangwan and M. C. Hersam, Electronic Transport in Two-Dimensional Materials, *Annu. Rev. Phys. Chem.*, 2018, **69**(1), 299–325, DOI: 10.1146/annurev-physchem-050317-021353.
22 F. Bonell, A. Marty, C. Vergnaud, V. Consonni, H. Okuno, A. Ouerghi, H. Boukari and M. Jamet, High Carrier Mobility in Single-Crystal PtSe 2 Grown by Molecular Beam Epitaxy on ZnO(0001), *2D Mater.*, 2022, **9**(1), 015015, DOI: 10.1088/2053-1583/ac37aa.
23 Y. Zhao, J. Qiao, Z. Yu, P. Yu, K. Xu, S. P. Lau, W. Zhou, Z. Liu, X. Wang, W. Ji and Y. Chai, High-Electron-Mobility and Air-Stable 2D Layered PtSe 2 FETs, *Adv. Mater.*, 2017, **29**(5), 1604230, DOI: 10.1002/adma.201604230.
24 M. W. Iqbal, M. Z. Iqbal, M. F. Khan, M. A. Shehzad, Y. Seo, J. H. Park, C. Hwang and J. Eom, High-Mobility and Air-Stable Single-Layer WS2 Field-Effect Transistors Sandwiched between Chemical Vapor Deposition-Grown Hexagonal BN Films, *Sci. Rep.*, 2015, **5**(1), 10699, DOI: 10.1038/srep10699.
25 H. Fang, S. Chuang, T. C. Chang, K. Takei, T. Takahashi and A. Javey, High-Performance Single Layered WSe 2 p-FETs with Chemically Doped Contacts, *Nano Lett.*, 2012, **12**(7), 3788–3792, DOI: 10.1021/nl301702r.
26 H. Li, X. Duan, X. Wu, X. Zhuang, H. Zhou, Q. Zhang, X. Zhu, W. Hu, P. Ren, P. Guo, L. Ma, X. Fan, X. Wang, J. Xu, A. Pan and X. Duan, Growth of Alloy MoS 2 x Se 2(1–x) Nanosheets with Fully Tunable Chemical Compositions and Optical Properties, *J. Am. Chem. Soc.*, 2014, **136**(10), 3756–3759, DOI: 10.1021/ja500069b.
27 R. Cheng, D. Li, H. Zhou, C. Wang, A. Yin, S. Jiang, Y. Liu, Y. Chen, Y. Huang and X. Duan, Electroluminescence and Photocurrent Generation from Atomically Sharp WSe_2/MoS_2 Heterojunction p–n Diodes, *Nano Lett.*, 2014, **14**(10), 5590–5597, DOI: 10.1021/nl502075n.
28 D. F. Plusquellic, K. Siegrist, E. J. Heilweil and O. Esenturk, Applications of Terahertz Spectroscopy in Biosystems, *ChemPhysChem*, 2007, **8**(17), 2412–2431, DOI: 10.1002/cphc.200700332.

 © 2026 The Author(s). Published by the Royal Society of Chemistry

Open Access Article. Published on 02 January 2026. Downloaded on 1/21/2026 12:58:23 AM.
This article is licensed under a Creative Commons Attribution-NonCommercial 3.0 Unported Licence.

29 B. Ferguson and X.-C. Zhang, Materials for Terahertz Science and Technology, *Nat. Mater.*, 2002, **1**(1), 26–33, DOI: 10.1038/nmat708.

30 E. Aytan, Y. S. Aytekin, O. Esenturk and M. V. Kahraman, Fabrication and Characterization of Photocrosslinked Phase Change Materials by Using Conventional and Terahertz Spectroscopy Techniques, *J. Energy Storage*, 2019, **26**, 100989, DOI: 10.1016/j.est.2019.100989.

31 Y. S. Aytekin, M. Köktürk, A. Zaczek, T. M. Korter, E. J. Heilweil and O. Esenturk, Optical Properties of Meloxicam in the Far-Infrared Spectral Region, *Chem. Phys.*, 2018, **512**, 36–43, DOI: 10.1016/j.chemphys.2018.04.022.

32 K. Abdukayumov, M. Mičica, F. Ibrahim, L. Vojáček, C. Vergnaud, A. Marty, J.-Y. Veuillen, P. Mallet, I. G. de Moraes, D. Dosenovic, S. Gambarelli, V. Maurel, A. Wright, J. Tignon, J. Mangeney, A. Ouerghi, V. Renard, F. Mesple, J. Li, F. Bonell, H. Okuno, M. Chshiev, J.-M. George, H. Jaffrès, S. Dhillon and M. Jamet, Atomic-Layer Controlled Transition from Inverse Rashba–Edelstein Effect to Inverse Spin Hall Effect in 2D PtSe 2 Probed by THz Spintronic Emission, *Adv. Mater.*, 2024, **36**(14), 2304243, DOI: 10.1002/adma.202304243.

33 P. A. Lane, P. D. Cunningham, J. S. Melinger, O. Esenturk and E. J. Heilweil, Hot Photocarrier Dynamics in Organic Solar Cells, *Nat. Commun.*, 2015, **6**, 7558, DOI: 10.1038/ncomms8558.

34 O. Esenturk, J. S. Melinger and E. J. Heilweil, Terahertz Mobility Measurements on Poly-3-Hexylthiophene Films: Device Comparison, Molecular Weight, and Film Processing Effects, *J. Appl. Phys.*, 2008, **103**(2), 023102, DOI: 10.1063/1.2828028.

35 O. Esenturk, J. S. Melinger, P. A. Lane and E. J. Heilweil, Relative Photon-to-Carrier Efficiencies of Alternating Nanolayers of Zinc Phthalocyanine and C 60 Films Assessed by Time-Resolved Terahertz Spectroscopy, *J. Phys. Chem. C*, 2009, **113**(43), 18842–18850, DOI: 10.1021/jp904107x.

36 R. Ulbricht, E. Hendry, J. Shan, T. F. Heinz and M. Bonn, Carrier Dynamics in Semiconductors Studied with Time-Resolved Terahertz Spectroscopy, *Rev. Mod. Phys.*, 2011, **83**(2), 543–586, DOI: 10.1103/RevModPhys.83.543.

37 C. J. Docherty, P. Parkinson, H. J. Joyce, M.-H. Chiu, C.-H. Chen, M.-Y. Lee, L.-J. Li, L. M. Herz and M. B. Johnston, Ultrafast Transient Terahertz Conductivity of Monolayer MoS 2 and WSe 2 Grown by Chemical Vapor Deposition, *ACS Nano*, 2014, **8**(11), 11147–11153, DOI: 10.1021/nn5034746.

38 M. T. Dau, C. Vergnaud, M. Gay, C. J. Alvarez, A. Marty, C. Beigné, D. Jalabert, J.-F. Jacquot, O. Renault, H. Okuno and M. Jamet, Van Der Waals Epitaxy of Mn-Doped MoSe2 on Mica, *APL Mater.*, 2019, **7**(5), 051111, DOI: 10.1063/1.5093384.

39 R. Salazar, S. Varotto, C. Vergnaud, V. Garcia, S. Fusil, J. Chaste, T. Maroutian, A. Marty, F. Bonell, D. Pierucci, A. Ouerghi, F. Bertran, P. Le Fèvre, M. Jamet, M. Bibes and J. Rault, Visualizing Giant Ferroelectric Gating Effects in Large-Scale WSe 2/BiFeO 3 Heterostructures, *Nano Lett.*, 2022, **22**(23), 9260–9267, DOI: 10.1021/acs.nanolett.2c02448.

40 C. Vergnaud, M.-T. Dau, B. Grévin, C. Licitra, A. Marty, H. Okuno and M. Jamet, New Approach for the Molecular Beam Epitaxy Growth of Scalable WSe 2 Monolayers, *Nanotechnology*, 2020, **31**(25), 255602, DOI: 10.1088/1361-6528/ab80fe.

41 E. Pavoni, E. Mohebbi, G. M. Zampa, P. Stipa, L. Pierantoni, E. Laudadio and D. Mencarelli, First Principles Study of WSe 2 and the Effect of V Doping on the Optical and Electronic Properties, *Mater. Adv.*, 2024, **5**(6), 2230–2237, DOI: 10.1039/D3MA00940H.

42 E. Pavoni, E. Mohebbi, P. Stipa, D. Mencarelli, L. Pierantoni and E. Laudadio, The Role of Zr on Monoclinic and Orthorhombic HfxZryO2 Systems: A First-Principles Study, *Materials*, 2022, **15**(12), 4175, DOI: 10.3390/ma15124175.

43 S. Smidstrup, T. Markussen, P. Vancraeyveld, J. Wellendorff, J. Schneider, T. Gunst, B. Verstichel, D. Stradi, P. A. Khomyakov, U. G. Vej-Hansen, M.-E. Lee, S. T. Chill, F. Rasmussen, G. Penazzi, F. Corsetti, A. Ojanperä, K. Jensen, M. L. N. Palsgaard, U. Martinez, A. Blom, M. Brandbyge and K. Stokbro, QuantumATK: An Integrated Platform of Electronic and Atomic-Scale Modelling Tools, *J. Phys. Condens. Matter*, 2020, **32**(1), 015901, DOI: 10.1088/1361-648X/ab4007.

44 E. Pavoni, E. Mohebbi, D. Mencarelli, P. Stipa, E. Laudadio and L. Pierantoni, The Effect of Y Doping on Monoclinic, Orthorhombic, and Cubic Polymorphs of HfO2: A First Principles Study, *Nanomaterials*, 2022, **12**(23), 4324, DOI: 10.3390/nano12234324.

45 J. P. Perdew, K. Burke and M. Ernzerhof, Generalized Gradient Approximation Made Simple, *Phys. Rev. Lett.*, 1996, **77**(18), 3865–3868, DOI: 10.1103/PhysRevLett.77.3865.

46 M. J. van Setten, M. Giantomassi, E. Bousquet, M. J. Verstraete, D. R. Hamann, X. Gonze and G.-M. Rignanese, The PseudoDojo: Training and Grading a 85 Element Optimized Norm-Conserving Pseudopotential Table, *Comput. Phys. Commun.*, 2018, **226**, 39–54, DOI: 10.1016/j.cpc.2018.01.012.

47 F. Wooten and S. P. Davis, Optical Properties of Solids, *Am. J. Phys.*, 1973, **41**(7), 939–940, DOI: 10.1119/1.1987434.

48 K. Mondal, A. Haldar, A. Pramanik, R. Layek, D. Banerjee, V. R. Soma, S. Pal and P. Kumbhakar, Enhanced Femtosecond Nonlinear Optical Susceptibility and Terahertz Conductivity in MoSe 2 -Noble Metal Nanocomposites, *Adv. Opt. Mater.*, 2024, **12**(23), 2401138, DOI: 10.1002/adom.202401138.

49 S. Liu, X. Xiong, X. Wang, X. Shi, R. Huang and Y. Wu, Hole Mobility Enhancement in Monolayer WSe2 P-Type Transistors through Molecular Doping, *Sci. China Inf. Sci.*, 2024, **67**(6), 160406, DOI: 10.1007/s11432-024-4032-6.

50 C. Zhou, Y. Zhao, S. Raju, Y. Wang, Z. Lin, M. Chan and Y. Chai, Carrier Type Control of WSe 2 Field-Effect Transistors by Thickness Modulation and MoO 3 Layer Doping, *Adv. Funct. Mater.*, 2016, **26**(23), 4223–4230, DOI: 10.1002/adfm.201600292.

Open Access Article. Published on 02 January 2026. Downloaded on 1/21/2026 12:58:23 AM.
This article is licensed under a Creative Commons Attribution-NonCommercial 3.0 Unported Licence.

51 X. Chen, S. Zhang, L. Wang, Y.-F. Huang, H. Liu, J. Huang, N. Dong, W. Liu, I. M. Kislyakov, J. M. Nunzi, L. Zhang and J. Wang, Direct Observation of Interlayer Coherent Acoustic Phonon Dynamics in Bilayer and Few-Layer PtSe 2, *Photonics Res.*, 2019, **7**(12), 1416, DOI: 10.1364/PRJ.7.001416.

52 H. Liu, Z. Chen, X. Chen, S. Chu, J. Huang and R. Peng, Terahertz Photodetector Arrays Based on a Large Scale MoSe 2 Monolayer, *J. Mater. Chem. C*, 2016, **4**, 9399, DOI: 10.1039/c6tc02748b.

53 J. Fu, W. Xu, X. Chen, S. Zhang, W. Zhang, P. Suo, X. Lin, J. Wang, Z. Jin, W. Liu and G. Ma, Thickness-Dependent Ultrafast Photocarrier Dynamics in Selenizing Platinum Thin Films, *J. Phys. Chem. C*, 2020, **124**(19), 10719–10726, DOI: 10.1021/acs.jpcc.0c01509.

54 L. Zhang, Z. Chen, R. Zhang, Y. Tan, T. Wu, M. Shalaby, R. Xie and J. Xu, Direct Observation of Charge Injection of Graphene in the Graphene/WSe 2 Heterostructure by Optical-Pump Terahertz-Probe Spectroscopy, *ACS Appl. Mater. Interfaces*, 2019, **11**(50), 47501–47506, DOI: 10.1021/acsami.9b13996.

55 L. Ansari, S. Monaghan, N. McEvoy, C. Ó. Coileáin, C. P. Cullen, J. Lin, R. Siris, T. Stimpel-Lindner, K. F. Burke, G. Mirabelli, R. Duffy, E. Caruso, R. E. Nagle, G. S. Duesberg, P. K. Hurley and F. Gity, Quantum Confinement-Induced Semimetal-to-Semiconductor Evolution in Large-Area Ultra-Thin PtSe2 Films Grown at 400 °C, *npj 2D Mater. Appl.*, 2019, **3**(1), 33, DOI: 10.1038/s41699-019-0116-4.

56 J. Gusakova, X. Wang, L. L. Shiau, A. Krivosheeva, V. Shaposhnikov, V. Borisenko, V. Gusakov and B. K. Tay, Electronic Properties of Bulk and Monolayer TMDs: Theoretical Study Within DFT Framework (GVJ-2e Method), *Phys. Status Solidi*, 2017, **214**(12), 1700218, DOI: 10.1002/pssa.201700218.

 © 2026 The Author(s). Published by the Royal Society of Chemistry